Supplementary Information for

Field-free Josephson diode effect in $NbSe_2$ van der Waals junction

Jiaxiang Ma[1], Huiyu Wang[2], Weizhuang Zhuo[2], Bin Lei[3], Shuai Wang[3], Wenxiang Wang[2], Xin-Yu Chen[1], Zhen-Yu Wang[2], Binghui Ge[3], Zhen Wang[2], Jing Tao[2], Kun Jiang[4], Ziji Xiang[1,5], and Xian-Hui Chen[1,2,5]

[1] *Hefei National Research Center for Physical Sciences at the Microscale, University of Science and Technology of China, Hefei 230026, China*

[2] *Department of Physics, University of Science and Technology of China, Hefei 230026, China*

[3] *Institutes of Physical Science and Information Technology, Anhui University, Hefei 230601, China*

[4] *Beijing National Laboratory for Condensed Matter Physics and Institute of Physics, Chinese Academy of Sciences, Beijing 100190, China.*

[5] *Hefei National Laboratory, University of Science and Technology of China, Hefei 230088, China.*

Supplementary Note 1: Experimental setups for different measurements

Here we introduce all the experimental setups used in our measurements and focused on the different methods for applying current. As shown in the circuit diagram in Fig. S1a, for the temperature dependence of resistance measurements, we used the internal oscillator in SR830 to apply an AC voltage ($f = 19.711$ Hz) of 2 Vrms to a 0.2 MΩ resistor R_1 (which is in series with the device, but the resistance is much larger than the device) to generate an AC current of around 10 μA. The AC voltage signal across the junction was measured using the same SR830 lock-in amplifier. In the measurement of voltage versus current characteristic (I-V curve), a sweeping DC current was applied directly by a current source Keithley 6221 ($R_2 = 100\,\Omega$ is merely a protective resistor), and the voltage signal was measured using a Keithley 2182A nanovoltmeter as shown in the Fig. S1b.

For the dV/dI measurements, we chose to use a current source to apply the sweeping DC current as well, as illustrated in Fig. S1c. Simultaneously, a small AC excitation (10 nA and 277 Hz) was supplied by SR830 combined with a 1 MΩ resistor. To obtain the dV/dI, the AC voltage signal was measured by SR830 after amplifying by the SR560 preamplifier. Note that a current source has very large output resistance (for instance, on the order of $10^{14}\,\Omega$ for the Keithley 6221 current source we used), thus the AC current flowing through the Keithley 6221 to the ground can be ignored.

In dV/dI measurements, we used two sets of filters: (i) four homemade silver-epoxy low-pass filters with cut-off frequency around 470 kHz were added connected to the BNC ports on the break-out box that correspond to the voltage and current leads on the device, as marked with red circles in Fig. S1c; (ii) we used the built-in filter of the preamplifier SR560, which was set to low-pass mode with cut-off frequency of 10 kHz. For the temperature dependence of resistance measurements, we used only the homemade low-pass filters.

Supplementary Note 2: Excluding the possible extrinsic effects from electric circuit configurations

Besides the residual flux, the possible artificial effects of experimental setups or bad circuit designs may also contribute to a spurious nonreciprocity in transport properties. To investigate this possible contribution, we performed the following experiments:

1. *Contact of electrodes.* As shown in Fig. 1, there are eight electrodes on each device, only four of them were used for transport measurements. In practice, we chose the

electrodes with lower contact resistance on each $NbSe_2$ flake. To excluding the influence from the electrodes, we tried different electrode permutations on device 1 and the results are summarized in Fig. S2. The two groups of data exhibit essentially identical JDE at zero field. This verifies the negligible influence of changing electrodes upon the experimental results.

2. *Circuit configurations*. All the *I*-*V* curves above were measured by the same electric circuit configurations in Fig. S1, with a resistor on one side and ground on another side of device. To investigate the possible contribution from the unintentional bias effect of this circuit configuration, we fabricated a new $NbSe_2$/$NbSe_2$ junction (device 7) using the same techniques; it displays field-free JDE. Subsequently, we measured the *I*-*V* characteristics with three different designs of experimental setups: (i) The same circuit as the Fig. S1b (Figs. S3a-c); (ii) the resistor R and ground switch side with respect to the device (Figs. S3d-f); (iii) two identical resistors at the source and drain of the device, respectively (Figs. S3g-i). All the measurements yielded highly consistent and repeatable results without dependence on circuit design, indicating that the JDE is an intrinsic property of the device which is not sensitive to artificial bias conditions.

3. *The current leakage to ground*. It is inevitable to introduce potential difference (between device and the ground/environment) to device when we input current for I-V curve measurements. If the device's insulation to the ground is not good enough, there will be current leakage to the ground and may cause a three-terminal device (triode), in which nonreciprocity is commonly expected. To examine such possibility, we tested the setup's insulation to ground. As shown in Fig. S4a, we applied a 10 V (to ground) DC voltage to the device and measured the current by a Keithley 6482 picoammeter. (The internal resistances of the voltage source and picoammeter are negligible, and R = 100 Ω is merely a protective resistor.) The detected current was lower than 0.2 nA (Fig. S4b), which is 6 orders of magnitude lower than our measurement current; the resistance to ground is thus determined to be larger than $10^{10}\,\Omega$. Therefore, the current leakage to ground is negligible and the JDE in our $NbSe_2$ van der Waals junctions is not caused by the unintentional realization of a three-terminal device.

In addition, we point out that the devices showing absence of zero-field JDE (Fig. S8) were also measured with the same circuit illustrated in Fig. S1b, suggesting that the measurement circuit itself does not introduce extrinsic JDE signal. This argument strengthens our claim that our observations reflect the intrinsic field-free JDE in the $NbSe_2/NbSe_2$ junctions instead of the extrinsic effects stemming from experimental setups.

Supplementary Note 3: Excluding the possible influence of residual flux in the magnet coil and the trapped vortices in devices

Josephson junctions are usually very sensitive to the presence of external magnetic flux. Unfortunately, the residual field flux is almost inevitable in superconducting magnet coils. It is very important to investigate the effects of this residual flux, as well as the feasible trapped vortices in the device introduced during the field ramping process. To minimize their influence, we ensured that (i) all the zero-field I-V curves were measured after a zero-field cooling (from a temperature above T_c down to 2 K) to eliminate the trapped vortices in the device; (ii) each time after field application, we ramped the field down to zero using an oscillation mode to diminish the remanent flux trapped in the coil. To examine the effectiveness of these procedures, we measured device 1 after applying a large H of 5 T and ramping to zero field in the oscillation mode, the I-V curves collected before and after such field ramping are almost identical without discernible changes, see Figs. S5a and b. This proves that the trapped-flux effect at zero field is sufficiently small.

We have also calibrated the trapped residual flux in our superconducting magnet using a high precision Hall probe (MCHD800S-LT, CH-Magnetoelectricity Technology Co.,Ltd.). Fig. S5c shows that remanent field is constantly within ±0.4 mT for 15 times of field ramping (down to zero). In Fig. 5b, the nonreciprocal component $\Delta I_c \approx$ -20 μA persists within a field range of ±5 mT, which cannot be assigned to the outcome of such a small remanent field. Moreover, this residual flux will be either positive or negative after field ramping (as shown in Fig. S5c), thus the ΔI_c of remnant-field-reduced JDE will have an arbitrary sign. However, the nonreciprocity of device 1 never changes its sign after field sweeps, inconsistent with the expectation for a phenomenon caused by the random residual flux.

In addition, if there is trapped vortex in devices, it will induce flux offset and shift the Fraunhofer pattern along the horizontal axis. In this sense, the symmetric H dependence of I_c in device 2 (Supplementary Fig. S12) unambiguously excludes the trapped vortex in our devices as the origin of field-free JDE.

Supplementary Note 4: Existing proposals for zero-field JDE

Here we briefly discuss the presently available proposals for zero-field JDE. Spontaneous TRSB has been widely reported in twisted bilayer systems and the zero-field SDE has been also observed in twisted trilayer and bilayer graphene devices [1–3]. Since the TRSB therein is resulted from twist-angle-driven orbital magnetism or valley polarization, the the resistance and I-V profiles correspondingly exhibit a hysteretic behavior during up and down sweeps of H and the zero-field SDE can only be observed after training with an external magnetic field. However, in our $NbSe_2$/$NbSe_2$ junctions, the zero-field JDE can appear immediately after zero-field cooling without any magnetic training. Additionally, after a training process of ramping the field up to 5 T then back to zero, the I-V curves remain almost unchanged (Supplementary Figs. S5a-b). These distinct field dependences compared with the graphene-based devices strongly imply the different physical origins of the TRSB. We further tested the response of I_c to magnetic field orientations and the sweeping directions in device 8 (4.3 nm/4.3 nm, exhibiting field-free JDE). As shown in Supplementary Figs. S6a and b, I_c exhibits a larger response to out-of-plane H ($H_\perp$) compared to in-plane H ($H_{//}$). The evolutions of I_c with two field orientations share similarities: I_c initially undergoes a gradual decay with increasing H and the difference $\Delta I_c > 0$ diminishes progressively. Nonzero ΔI_c persists up to approximately 100 mT under out-of-plane H (marked by red arrows in Fig. S6b), manifesting a faster suppression of the zero-field JDE in this configuration. The anisotropic response of ΔI_c to H is more likely originating from the superconductivity of $NbSe_2$ thin flakes. We have also measured I_c of device 8 with out-of-plane H sweeping from -150 mT to 150 mT and back to -150 mT. As shown in Fig. S6c, I_{c+} is independent of sweeping direction and shows non-hysteretic behavior, in sharp contrast to the above-mentioned characteristics of twisted graphene devices. These results and EBSD experiment (Fig. S7) suggest that the spontaneous TRSB in our devices has a distinct origin from the twisted systems.

Alternatively, recent theoretical efforts establish that the zero-field SDE can emerge from macroscopic TRSB in a non-equilibrium steady state, triggered by current dissipation [4, 5]. This mechanism depends on some prerequisites (e.g., strong electron correlation [4], or the special case that a vertical electric field applied to a bilayer system [5]). A latest experimental observation of field-free SDE in $PbTaSe_2$ nanoflakes has been attributed to such scenario, owing to interplay between electron correlation (which is indeed not naturally expected in that material) and dissipation [6]. As $NbSe_2$ is free of strong electron correlations, we do not expect a straightforward interpretation down this way either, and further investigations are still needed.

---

[1] Kuiri, M. et al. Spontaneous time-reversal symmetry breaking in twisted double bilayer graphene. *Nature Communications* **13,** 6468 (2022).

[2] Díez-Mérida, J. et al. Symmetry-broken Josephson junctions and superconducting diodes in magic-angle twisted bilayer graphene. *Nature Communications* **14,** 2396 (2023).

[3] Lin, J.-X. et al. Zero-field superconducting diode effect in small-twist-angle trilayer graphene. *Nature Physics* **18,** 1221-1227 (2022).

[4] Morimoto, T. & Nagaosa, N. Nonreciprocal current from electron interactions in noncentrosymmetric crystals: roles of time reversal symmetry and dissipation. *Scientific Reports* **8,** 2973 (2018).

[5] Daido, A. & Yanase, Y. Unidirectional superconductivity and superconducting diode effect induced by dissipation. *Physical Review B* **111,** L020508 (2025).

[6] Liu, F. et al. Superconducting diode effect under time-reversal symmetry. *Science Advances* **10,** eado1502 (2024).

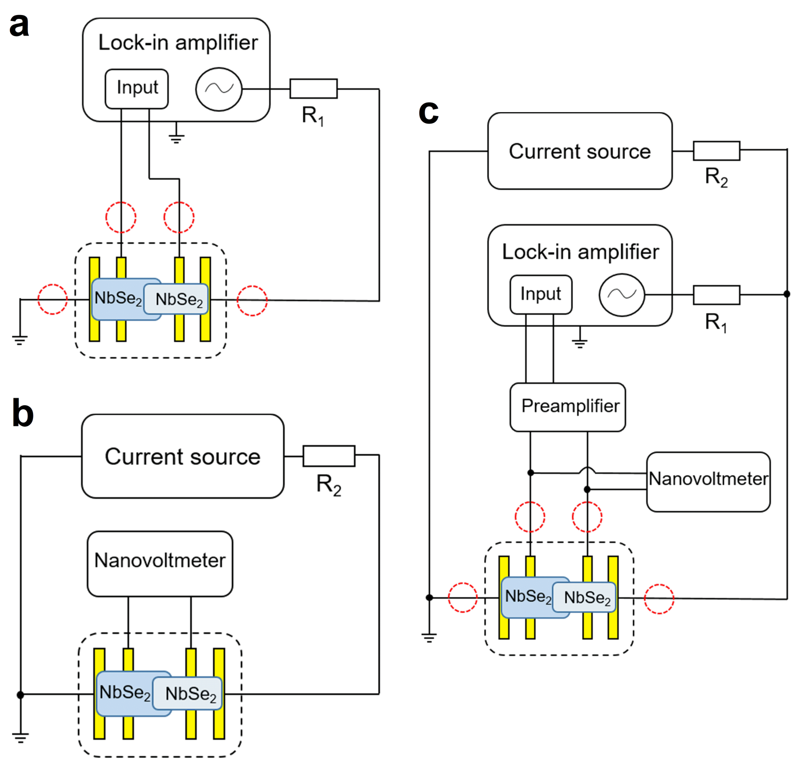

Fig. S1. **Schematic circuit diagrams of our measurements.** **a** Circuit for the temperature dependence of resistance measurement. The cryogenic chamber is marked as the black dashed box, and the dashed red circles outside the cryogenic chamber are homemade low-pass filters. **b,c** Circuits for the I-V curve and $\mathrm{d}V/\mathrm{d}I$ measurements.

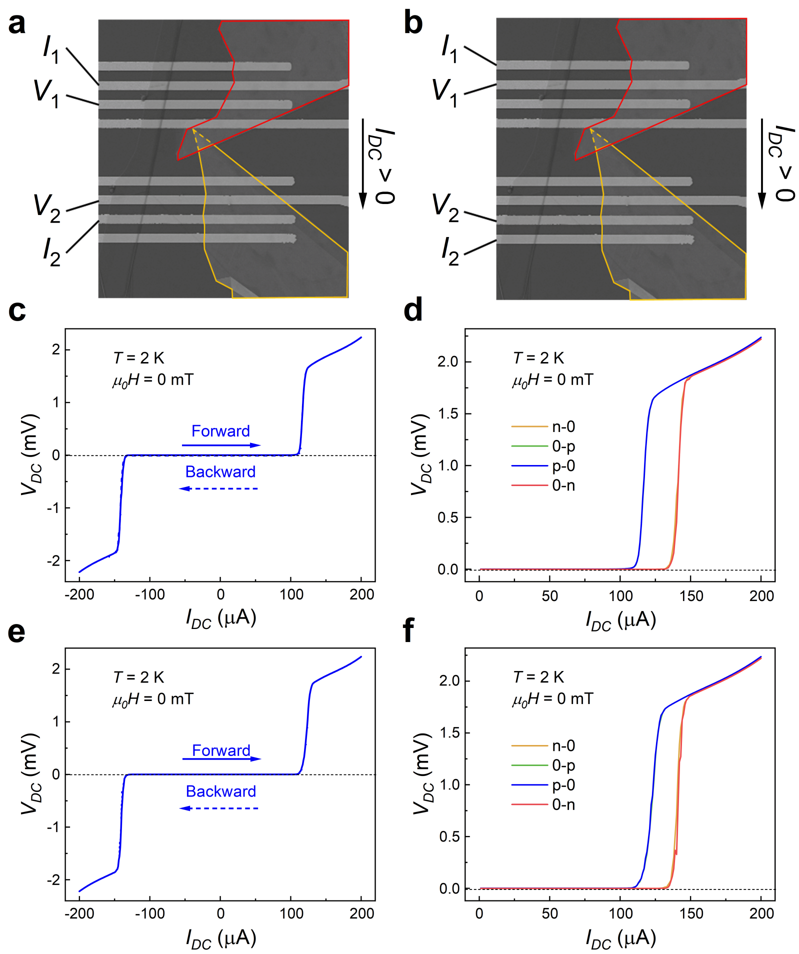

Fig. S2. **Test of different electrode permutations.** **a** The electrodes on device 1 that were used for collecting the measurement results in Figs. 2-5. **b** To test the effect of switching contacts, we chose another set of electrodes on device 1 and repeated measurements. The positive direction of I_{DC} is marked with arrows in **a**,**b**. **c**,**d** I-V curves in Fig. 2 of the main text (measured by the electrode permutation in **a**). **e**,**f** I-V curves we measured by the electrode permutation in **b**.

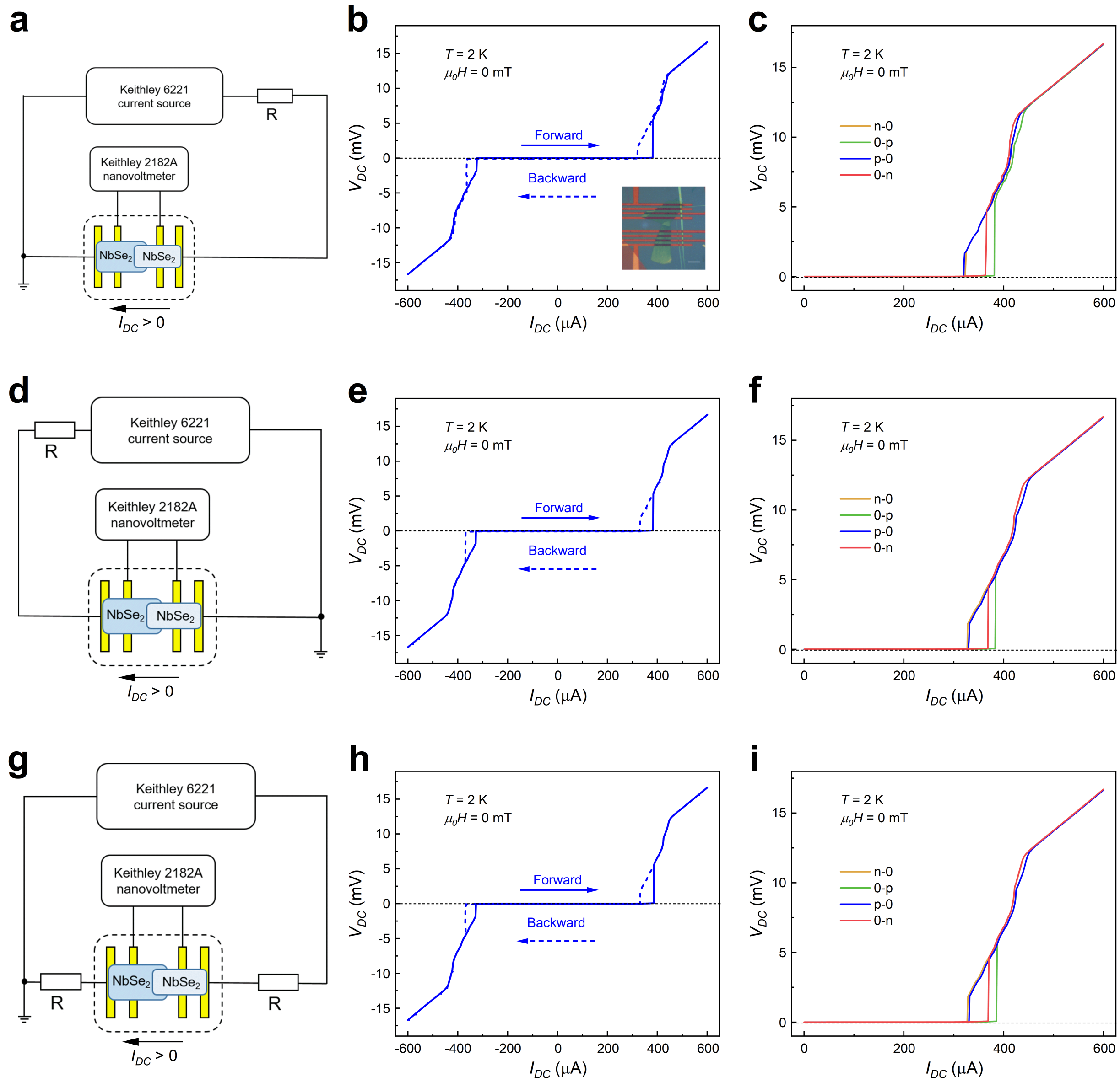

Fig. S3. *I-V* **curves of device 7 measured by different setups. b,c** were measured with the circuit in **a**, the same with device 1 in Figs. 2-5. Inset of **b** shows the optical micrograph of device 7 and the scale bar labels 10 µm. **e,f** and **h,i** were measured with the circuit in **d** and **g**, respectively. R is a protective resistor of 1 kΩ and the positive direction of I_{DC} is marked with arrows in **a,d,g**.

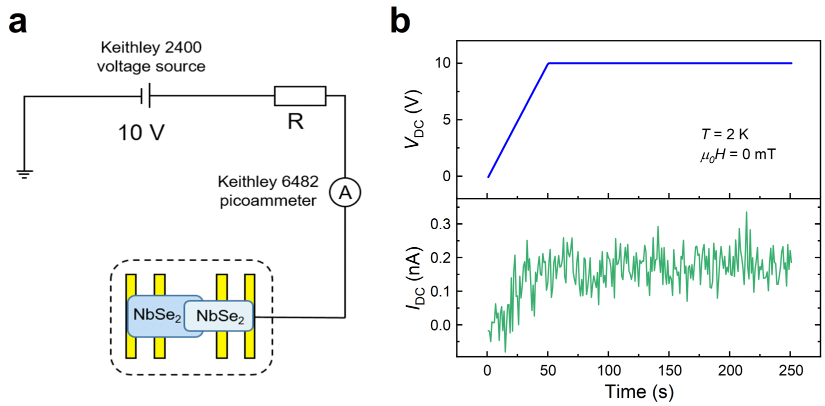

Fig. S4. **Test of the insulation between the device and ground. a** Circuit for the insulation test. **b** DC voltage applied between the device and ground (the top panel) and the current leakage to ground (the bottom panel).

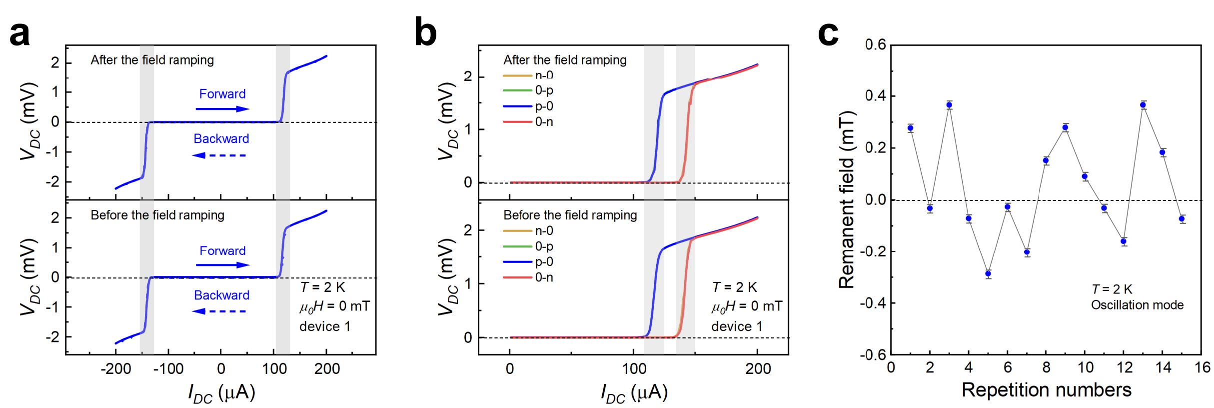

Fig. S5. **Test of the possible influence of residual flux. a,b** The *I*-*V* curves of device 1 measured after and before the field ramping. **c** Calibration of trapped flux in the superconducting magnetic for 15 down-ramps of magnetic field.

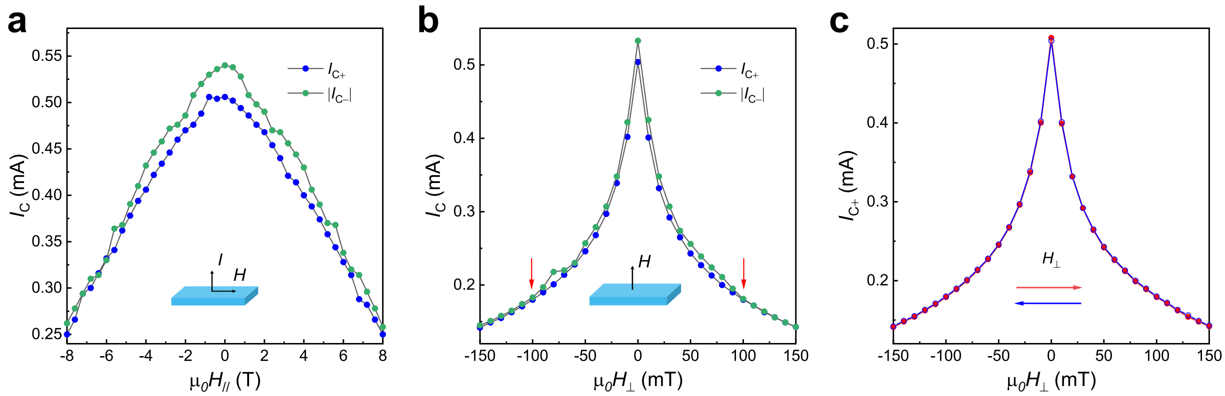

Fig. S6. **Response of JDE under different magnetic field orientations and sweeping directions.** H dependence of I_c with H applied in-plane (**a**) and out-of-plane (**b**) measured in device 8 (4.3 nm/4.3 nm). The directions of H and Josephson tunneling current (I) are indicated in the inset sketches. **c** I_{c+} as a function of out-of-plane H measured in device 8 with H sweeping up (red) and down (blue).

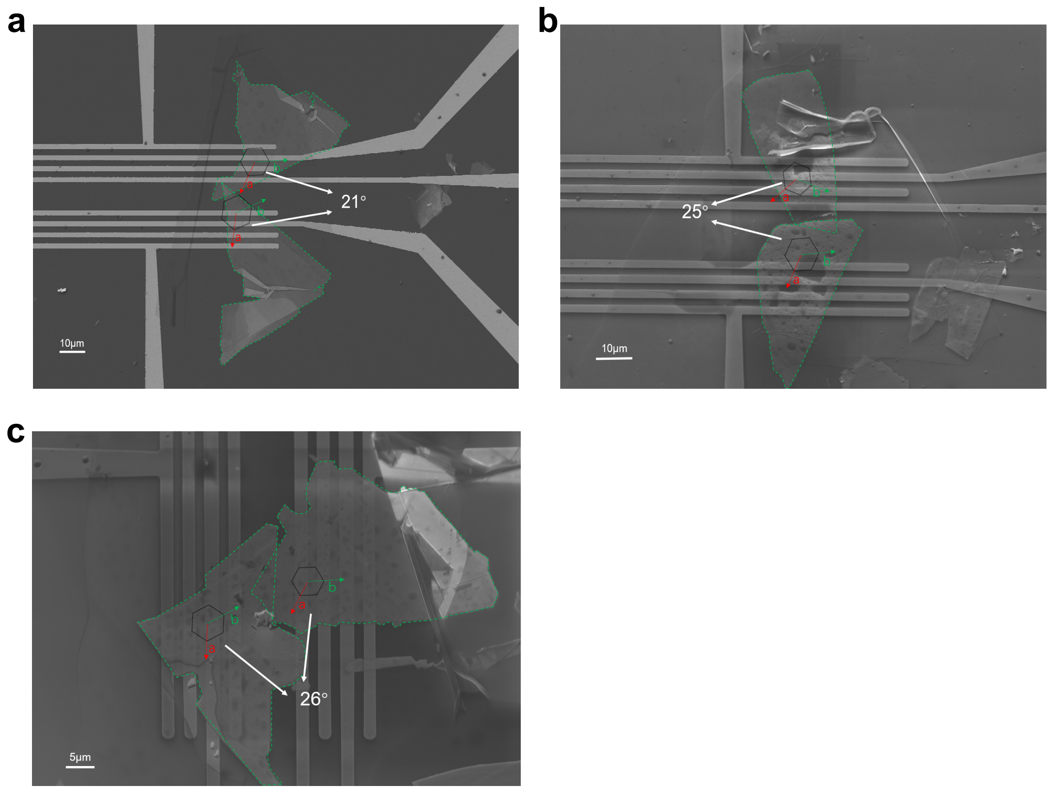

Fig. S7. **The EBSD results of device 1,2 and 6. a,b** The SEM images of device 1 and 2. The $NbSe_2$ flakes are highlighted with green dashed lines and the crystal orientations from EBSD are illustrated with black hexagons. The twist angles of device 1 and 2 are 21° and 25°, respectively. **c** The SEM image and EBSD result of device 6, with the twist angle of 26°.

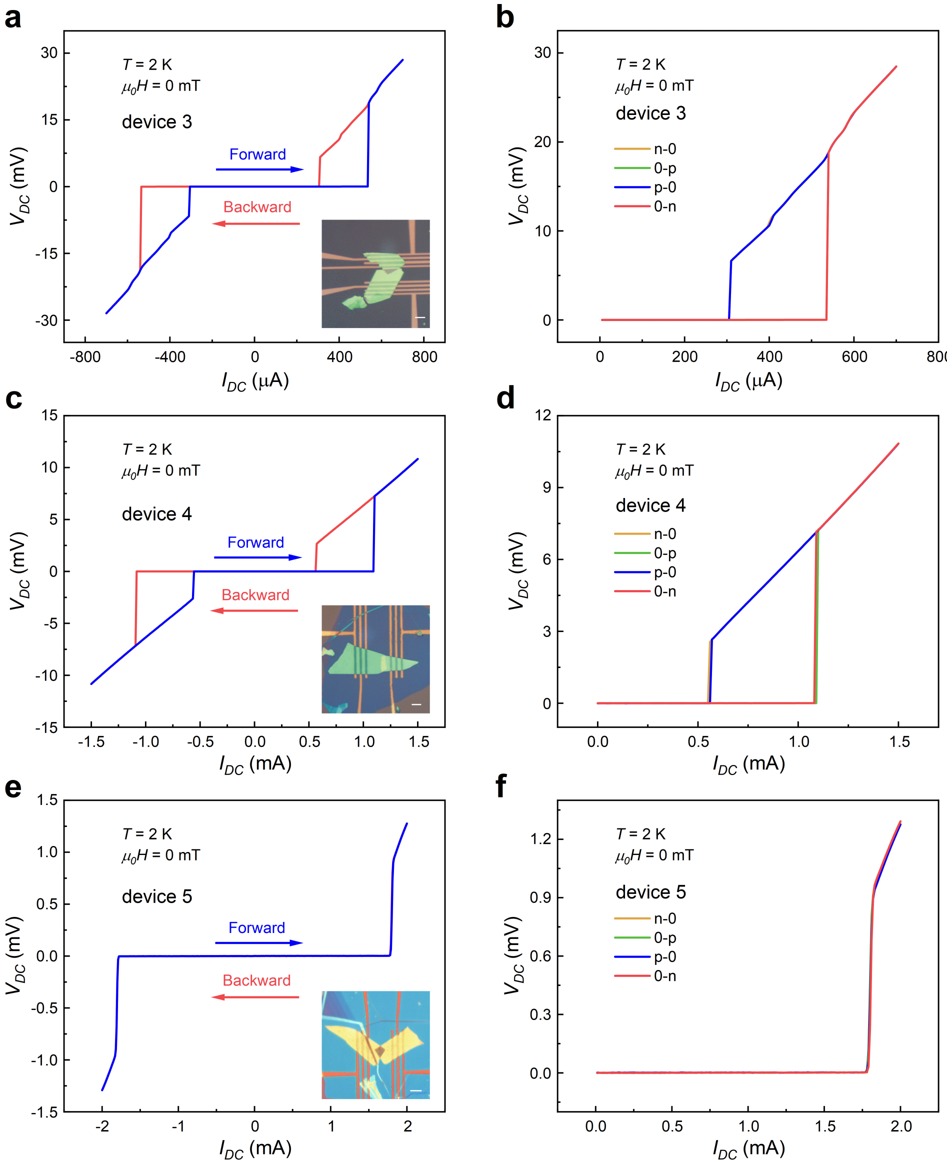

Fig. S8. **The I-V curves of JJs fabricated using thick $NbSe_2$ flakes. a,c,e** The I-V curves of device 3, 4 and 5 which are all composed of thick $NbSe_2$ flakes (range of 30-45 nm) at 2 K and zero field. The scale bar labels 10 μm in the insets.**b,d,f** The absolute values of the I-V curves of device 3, 4 and 5, respectively. They all show reciprocal behaviors with the same I_{c+} and $|I_{c-}|$.

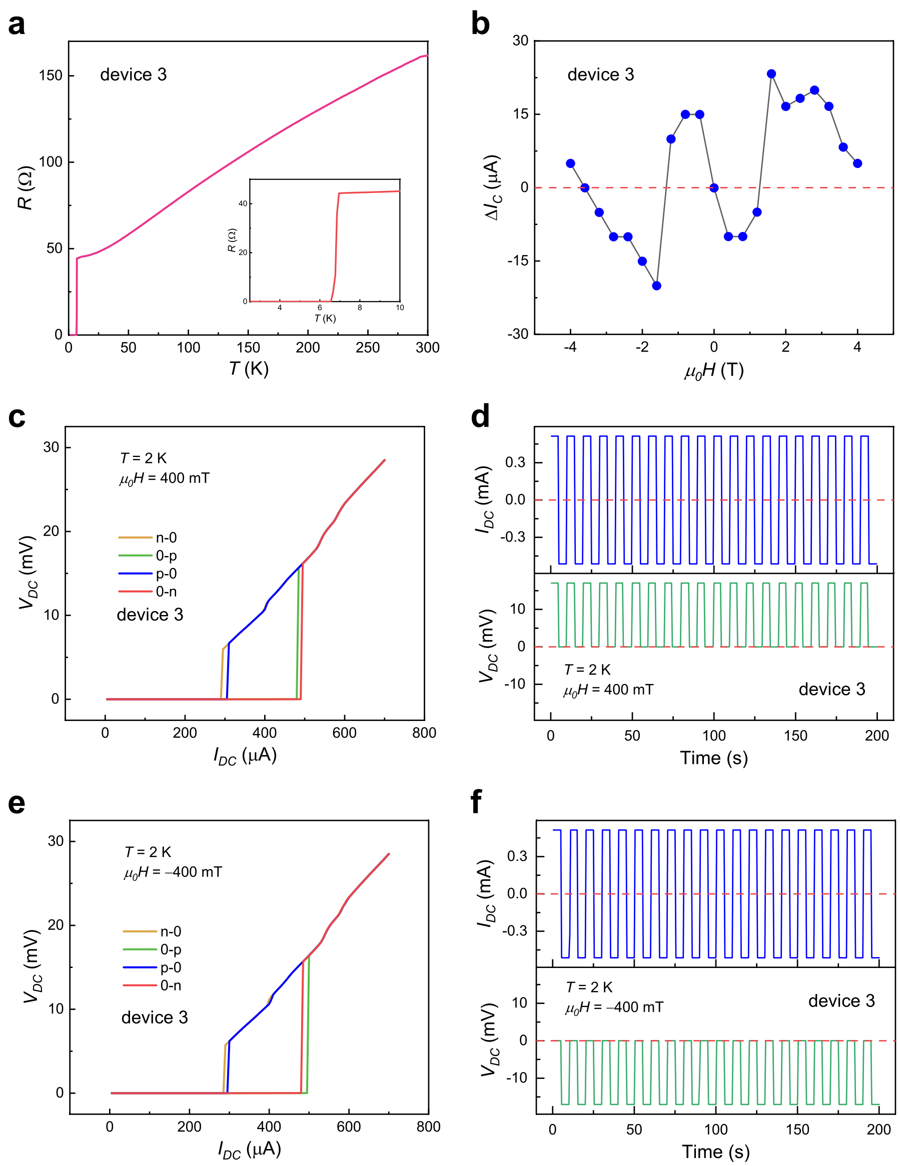

Fig. S9. **Basic characteristics and the field-induced JDE of device 3. a** The temperature-dependent resistance of device 3, showing a sharp superconducting transition at around 6.9 K. **b** The ΔI_c versus the in plane magnetic field, showing centrosymmetry relative to the magnetic field, which is different from device 1 and 2. **c,e** The absolute values of the *I*-*V* curves of device 3 at 400 and -400 mT, respectively. **d,f** The half-wave rectification of device 3 at 400 and -400 mT with the same square-wave current (0.513 mA and 0.1 Hz). Notably, device 3 shows the opposite response to the same square-wave current at 400 and -400 mT. When the current is positive, the junction voltage is a positive finite value (17 mV) at 400 mT but near zero at -400 mT. When the current switches to negative, the junction voltage is near zero at 400 mT but a negative finite value (-17 mV) at -400 mT. The centrosymmetry behavior versus field shows good agreement with **b**.

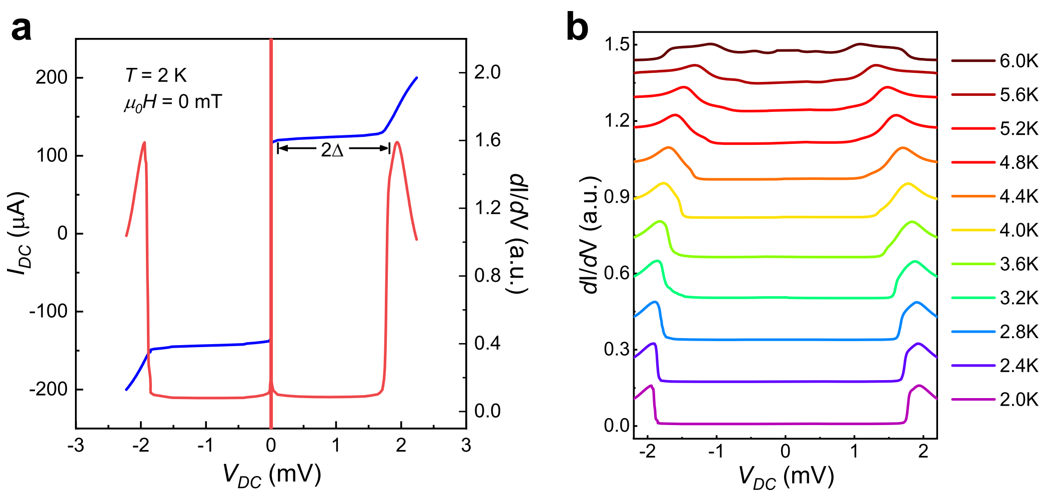

Fig. S10. **The differential conductance of device 1.** **a** Differential conductance along with I-V curve at 2 K and zero field. The peaks of differential conductance emerge at the value twice of superconducting gap, attributable to the tunneling of Cooper pairs. **b** Temperature dependence of the differential conductance. As the temperature increasing, the positions of the peaks move toward zero.

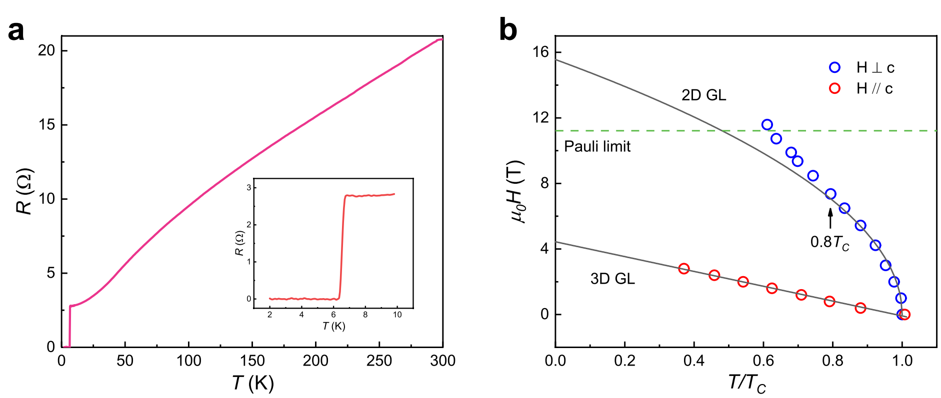

Fig. S11. **The superconductivity of $NbSe_2$ flake in device 1.** **a** The temperature-dependent resistance of $NbSe_2$ flake in device 1, showing a sharp superconducting transition at around 6.5 K. Inset, zoomed-in area of the superconducting transition. **b** The temperature dependence of the upper critical field of the $NbSe_2$ flake in device 1. The out of plane upper critical field is plotted with red circles which is linear versus magnetic field and fits well with the 3D Ginzburg–Landau model. The in plane upper critical field(blue circles) is fitted using the 2D Ginzburg–Landau model at $T > 0.8T_c$ and an upturn is observed at $0.8T_c$.

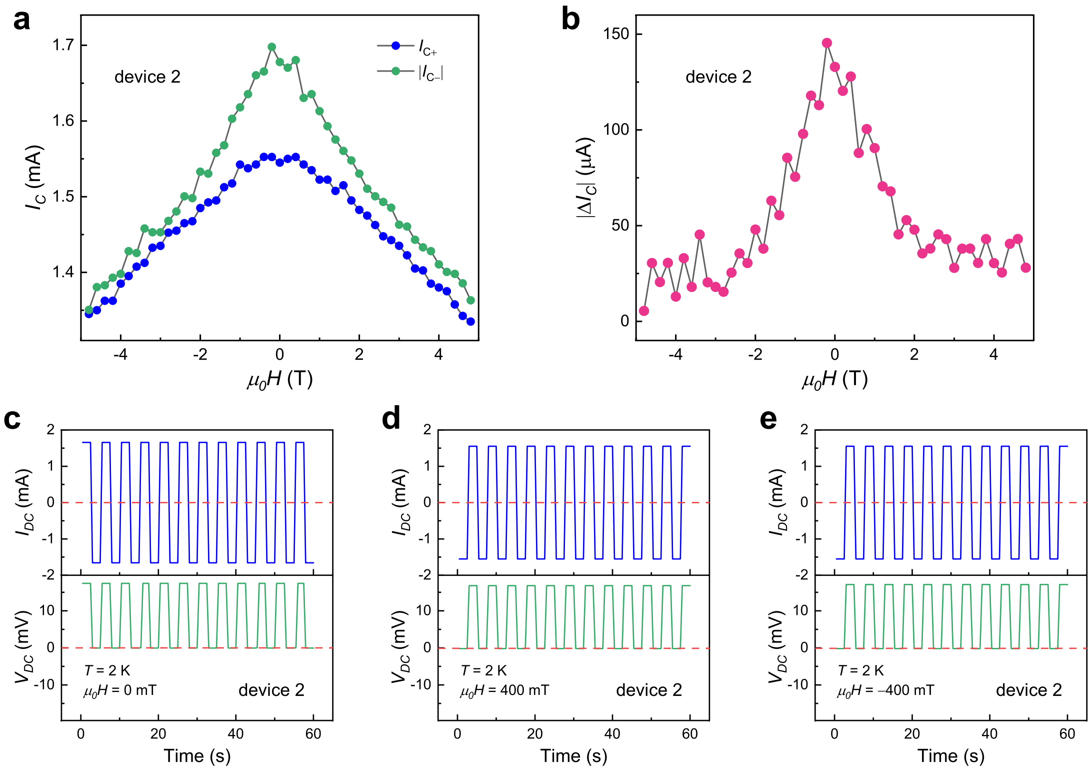

Fig. S12. **The magnetic field dependence of I_{c} and half-wave rectification of device 2. a** The $I_{\mathrm{c}+}$ and $|I_{\mathrm{c}-}|$ versus the in plane magnetic field. **b** The ΔI_{c} versus the in plane magnetic field, showing a symmetric behavior. **c** Half-wave rectification of device 2 at zero field. The blue line in the top panel shows a square-wave current with amplitude of 1.658 mA and a frequency of 0.2 Hz which was applied to device 2, and the green line in the bottom panel is the voltage measured in the junction. The red dashed lines indicate the zero value. The voltage is near zero when the current is negative and a finite value when the current switches to positive. **d,e** Half-wave rectification of device 2 at 400 mT and -400 mT, respectively. A square-wave current (1.551 mA and 0.2 Hz) was applied and the junction voltages show the same behavior at both 400 mT and -400 mT.

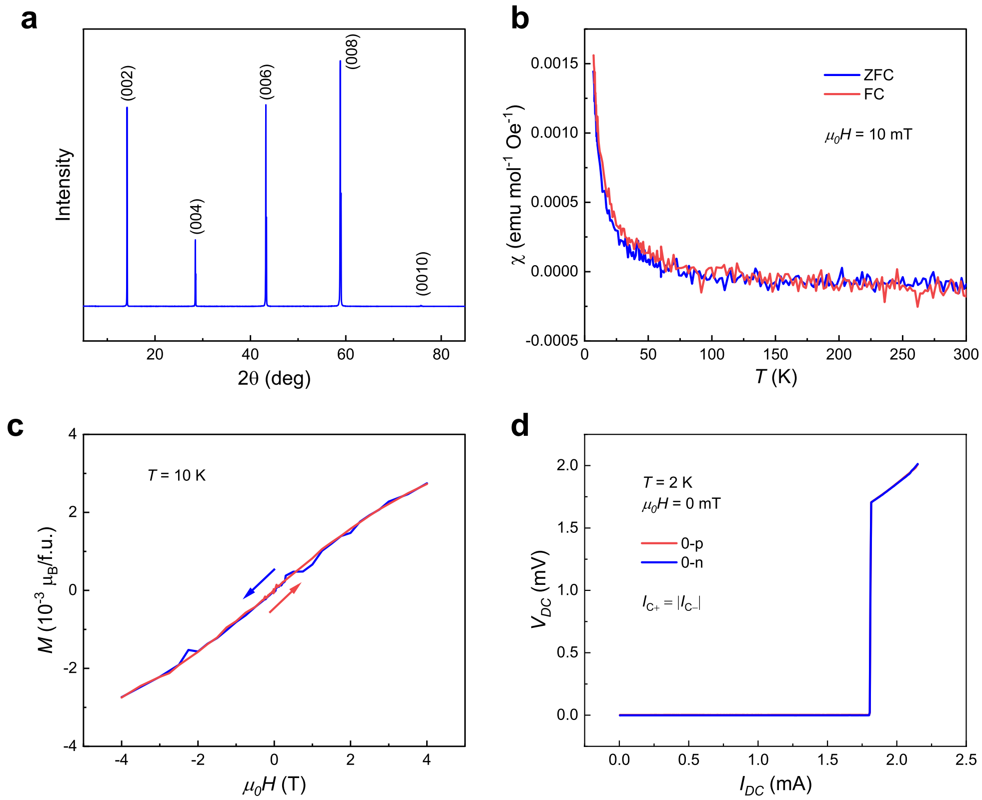

Fig. S13. **2H-NbSe$_2$ crystal characterization.** **a** X-ray Diffraction (XRD) spectroscopy of 2H-NbSe$_2$ single crystal used in our experiments. A lattice constant of 1.255 nm along c-axis can be obtained. **b** Temperature dependence of magnetic susceptibility $\chi(T)$ of 2H-NbSe$_2$ for 10-300 K. **c** Field dependence of magnetization $M(H)$ curves at 10 K. There is only a very small paramagnetic behavior from $\chi(T)$ and $M(H)$, implying no magnetic impurity in our crystal. **d** The absolute values of the I-V curve of NbSe$_2$ flake in device 1, showing a reciprocal behavior with the same I_{c+} and $|I_{c-}|$ at 0 mT.

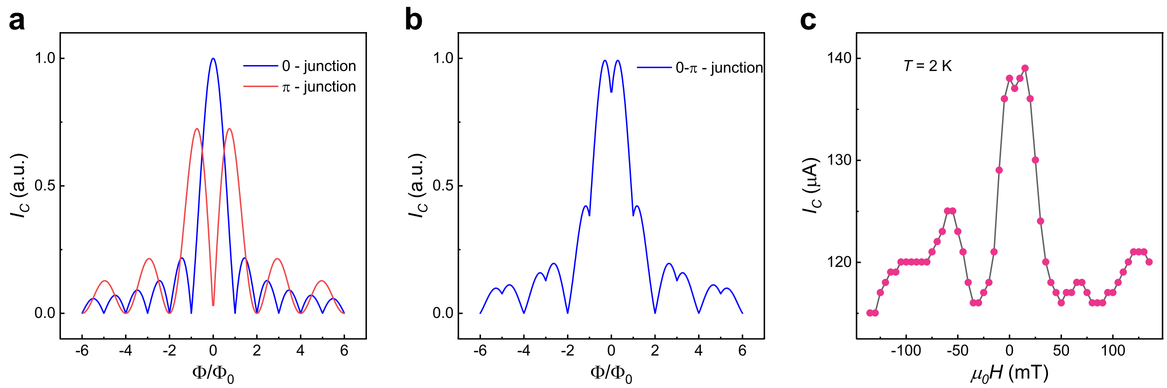

Fig. S14. **The critical supercurrents as a function of magnetic field for different type of JJs. a,b** Numerical modeling of the oscillatory patterns of critical current for 0, π, and 0–π mixed Josephson junctions. **c** The I_c versus field of device 1.

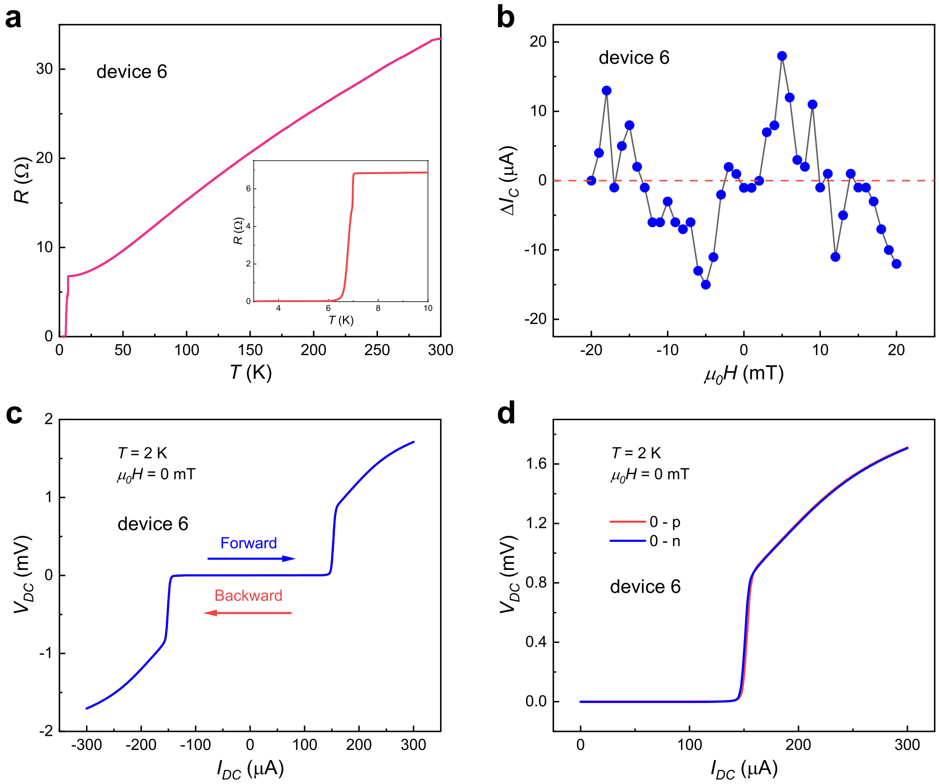

Fig. S15. **Basic characteristics of device 6 fabricated with thin $NbSe_2$ flakes (both around 6 nm).** **a** The temperature-dependent resistance of device 6, showing a sharp superconducting transition at around 6.7 K. **b** The ΔI_c versus the in plane magnetic field, showing centrosymmetry field dependence, the same as device 3. **c,d** The I-V curves of device 6. It shows reciprocal behavior with the same I_{c+} and $|I_{c-}|$.

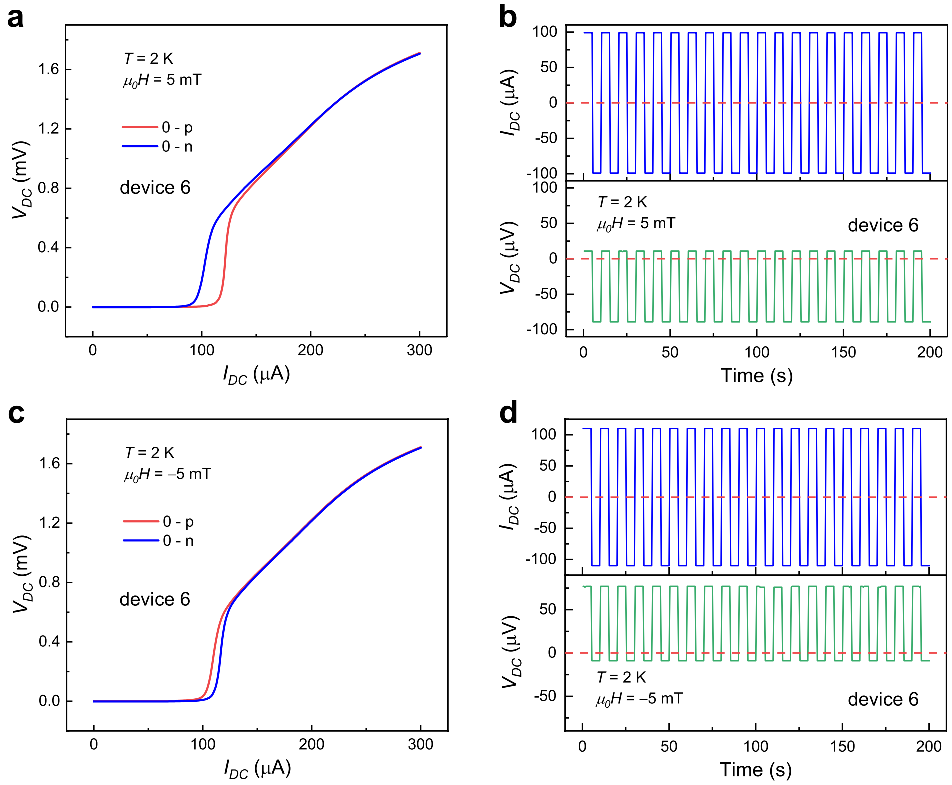

Fig. S16. **The field-induced JDE of device 6. a,c** The absolute values of the I-V curves of device 6 at 5 and -5 mT. **b,d** The half-wave rectification of device 6 at 5 and -5 mT, respectively, showing the same behavior with device 3.